ELSEVIER

Contents lists available at ScienceDirect

Journal of Environmental Management

journal homepage: www.elsevier.com/locate/jenvman



Research article

Mapping wetlands in Northeast China by using knowledge-based algorithms and microwave (PALSAR-2, Sentinel-1), optical (Sentinel-2, Landsat), and thermal (MODIS) images

Chenchen Zhang ^a, Xiangming Xiao ^{a,*}, Xinxin Wang ^b, Yuanwei Qin ^a, Russell Doughty ^c, Xuebin Yang ^d, Cheng Meng ^a, Yuan Yao ^a, Jinwei Dong ^e

ARTICLE INFO

Handling Editor: Lixiao Zhang

Keywords:

Seasonal open-canopy marsh Yearlong closed-canopy marsh Forest swamp Knowledge-based algorithm Google Earth engine

ABSTRACT

Wetlands are rich in biodiversity, provide habitats for many wildlife species, and play a vital role in the transmission of bird-borne infectious diseases (e.g., highly pathogenic avian influenza). However, wetlands worldwide have been degraded or even disappeared due to natural and anthropogenic activities over the past two centuries. At present, major data products of wetlands have large uncertainties, low to moderate accuracies, and lack regular updates. Therefore, accurate and updated wetlands maps are needed for the sustainable management and conservation of wetlands. Here, we consider the remote sensing capability and define wetland types in terms of plant growth form (tree, shrub, grass), life cycle (perennial, annual), leaf seasonality (evergreen, deciduous), and canopy type (open, closed). We identify unique and stable features of individual wetland types and develop knowledge-based algorithms to map them in Northeast China at 10 m spatial resolution by using microwave (PALSAR-2, Sentinel-1), optical (Landsat (ETM+/OLI), Sentinel-2), and thermal (MODIS land surface temperature, LST) imagery in 2020. The resultant wetland map has a high overall accuracy of >95%. There were a total 154,254 km² of wetlands in Northeast China in 2020, which included 27,219 km² of seasonal open-canopy marsh, 69,158 km² of yearlong closed-canopy marsh, and 57,878 km² of deciduous forest swamp. Our results demonstrate the potential of knowledge-based algorithms and integrated multi-source image data for wetlands mapping and monitoring, which could provide improved data for the planning of wetland conservation and restoration.

1. Introduction

Wetlands, characterized with a mix of plants, surface water, and/or water-saturated soils, provide vital habitats for various wildlife such as fishes, waterbirds, and frogs (Aiello-Lammens et al., 2011; Jansen and Healey, 2003; Murray et al., 2019), affect the atmosphere by sequestrating or emitting carbon (e.g., CO₂ and CH₄) (Brix et al., 2001; Lan et al., 2021; Picek et al., 2007; Tollefson, 2022), and play a significant role in the zoonotic disease transmission (Gilbert et al., 2008, 2014; Jourdain et al., 2007). However, over the last two centuries, wetlands

worldwide have been changing rapidly, driven by human activities and climate and hydrological changes, such as population growth, agriculture reclamation, warmer temperatures, and changing precipitation patterns (Chen et al., 2018; Gong et al., 2010; Richards and Friess, 2016). Several satellite-based global land cover data products (e.g., IGBP-DISCover and FROM-GLC) include a broad category for wetlands (Gong et al., 2013; Karra et al., 2021; Loveland et al., 2000; Zhang et al., 2021). However, their classification algorithms were not specifically designed for wetlands, leading to low to moderate accuracies in identifying wetlands. Furthermore, several wetland thematic products have

^a School of Biological Sciences, Center for Earth Observation and Modeling, University of Oklahoma, Norman, OK, 73019, USA

b Ministry of Education Key Laboratory for Biodiversity Science and Ecological Engineering, National Observations and Research Station for Wetland Ecosystems of the Yangtze Estuary, Institute of Biodiversity Science and Institute of Eco-Chongming, School of Life Sciences, Fudan University, Shanghai, 200438, China

^c College of Atmospheric and Geographic Sciences, University of Oklahoma, Norman, OK, 73019, USA

^d Geography and the Environment Department, Syracuse University, Syracuse, NY, 13244, USA

e Key Laboratory of Land Surface Pattern and Simulation, Institute of Geographic Sciences and Natural Resources Research, Chinese Academy of Sciences, Beijing, 100101. China

^{*} Corresponding author. School of Biological Sciences, University of Oklahoma, 101 David L. Boren Blvd., Norman, OK, 73019, USA. *E-mail address*: xiangming.xiao@ou.edu (X. Xiao).

been generated at regional and global scales (Darrah et al., 2019; Davidson and Finlayson, 2018; Pickens et al., 2020; Slagter et al., 2020), such as the 30 m national wetland map of China in 2015 (CAS_Wetlands) (Mao et al., 2020). However, most of these wetland products are not regularly updated, and thus cannot meet the need of updated and accurate wetland maps for wetland monitoring, protection, and management.

Optical images have been widely used for wetlands mapping (Table 1) (Davranche et al., 2010; Ghosh et al., 2016; Wang et al., 2020b, 2020d). Landsat images with a 30 m spatial resolution are an important data source for large-scale and historical wetland mapping due to their global coverage, long-term time series, suitable resolution, and free availability (Amani et al., 2019; Mao et al., 2020). Landsat has a 16-day revisit cycle and some events such as flooding in wetlands occur over short periods of time and are not frequently recorded by Landsat. Cloud, cloud shadow, and rainfall may limit the availability of good-quality Landsat observations for identifying specific events (Zhang et al., 2022). Moreover, small and narrow patches of natural wetlands with width <30 m are difficult to identify by Landsat images due to the mix of non-wetlands and wetlands within pixels. The new imagery from Sentinel-2A/B satellites with 10 m spatial resolution can partly reduce mixed pixel problem as compared to Landsat. Sentinel-2A/B images with 5-day revisit cycle, in combination with Landsat imagery, can increase the probability of cloud-free observations in the same period compared to Landsat alone (Pahlevan et al., 2019), which makes it possible to better capture phenological information or changes in land

Synthetic aperture radar (SAR) images offer an alternative data source for wetland mapping due to their independence from weather conditions and distinct backscattering characteristics for surface water and inundated vegetation (Amani et al., 2017; Li et al., 2020). L-band SAR systems with long wavelengths allow signals to penetrate vegetation canopies to map underlying emergent herbaceous and woody wetland vegetation through double-bounce backscatter (Townsend, 2002). With the launch of Sentinel-1, time series of high spatial resolution SAR data become available globally (Torres et al., 2012). The combination of SAR and optical data is expected to provide advantages of land surface reflectance and surface structure features, which has been demonstrated to improve classification accuracy of built-up area (Huang and Zhang, 2022; Qin et al., 2017), sugarcane (Wang et al., 2020a), mangrove (Chen et al., 2017), and paddy rice (Huang and Zhang, 2023). However, the potential of combining SAR and optical images for wetland mapping at large scales remains unexplored fully.

Wetland classification algorithms can be categorized into four approaches: (1) visual interpretation and classification, (2) data-based unsupervised classification, (3) information-based supervised classification, and (4) knowledge-based supervised classification (Table 1). The

visual interpretation and classification approach is time-consuming and labor-intensive. The data-based unsupervised classification approach calculates statistics of surface reflectance, vegetation indices, backscatter coefficient, and/or texture for all pixels in single- or multi-date images, and then uses clustering algorithms to generate various clusters that are later interpreted as different land cover types (Gong et al., 2010; Niu et al., 2009). The information-based supervised classification approach uses image data from regions of interest (ROIs) to train classification algorithms and then applies the trained algorithms to generate wetland maps (Han et al., 2018; Vo et al., 2013; Xing and Niu, 2019). This approach requires a large amount of high-quality training data for the specific land cover types being classified. The knowledge-based supervised classification approach analyzes time series image data of selected pixels for specific land cover types and identifies unique and stable optical and/or microwave characteristics of those land cover types, which is considered as knowledge. The knowledge (e.g., objectand sensor-specific phenological traits), along with associated decision trees and rule-based algorithms, is applied to identify specific land cover Several studies have highlighted the potential of knowledge-based algorithms in generating annual maps of plantations, crops, surface water, and coastal wetlands (Chen et al., 2017; Dong et al., 2013; Helman et al., 2015; Massey et al., 2017; Wang et al., 2020a, 2021; Xiao et al., 2005a, 2006; Zhang et al., 2023a). Despite these successful applications, the knowledge of inland wetlands is poorly explored and the knowledge-based algorithm has not been designed and applied for identifying and mapping inland wetlands.

Northeast China is renowned for its abundant wetland ecosystems, characterized by a high concentration and diversity of wetlands. Currently, 15 sites in this region have been listed as internationally important wetlands, accounting for 26% of China. In this study, we integrated all available microwave (PALSAR-2, Sentinel-1), optical (Landsat (ETM+/OLI), Sentinel-2), and thermal (MODIS land surface temperature) images over Northeast China in 2020 in Google Earth Engine (GEE) to (1) identify and evaluate unique and stable optical and/or microwave signatures of wetlands based on their biophysical features; (2) develop knowledge-based algorithms for wetland classification; and (3) apply and evaluate these algorithms to generate a wetland map at 10 m spatial resolution for Northeast China in 2020.

2. Materials and methods

2.1. Study area

Northeast China encompasses Heilongjiang, Jilin, and Liaoning Provinces, and four municipalities in eastern Inner Mongolia Autonomous Region (Supplementary Fig. 1). The region has a cold temperate and humid/sub-humid climate. Annual accumulated air temperatures

Table 1A sample list of publications on image data sources and algorithms for wetland mapping from previous studies.

Methods	Optical			SAR (RADARSAT,	Optical + SAR (MODIS,
	VHSR (<10 m; e.g., QuickBird, IKONOS, UAV)	HSR (10 m–30 m; e.g., SPOT-5, Landsat)	MSR (250 m–500 m; e.g., MODIS)	ERS-1, Sentinel-1)	Landsat, Sentinel-2, PALSAR, Sentinel-1)
Visual interpretation and classification	Liu et al. (2017)	Gong et al. (2010)			
Data-based unsupervised classification (e.g., K-means, ISODATA)		(Giri et al., 2015; Simard et al., 2008)		Parmuchi et al. (2002)	
Information-based supervised classification (e.g., MLC, NN, DT, SVM, RF) Knowledge-based supervised classification	(Wang et al., 2004, 2015)	(Amani et al., 2019; Davranche et al., 2010; Han et al., 2018; Mao et al., 2020; Vo et al., 2013) (Wang et al., 2020d, 2021; Zhang et al., 2020)	Xing and Niu (2019)	(Parmuchi et al., 2002; Simard et al., 2002)	(Mahdianpari et al., 2020; Niculescu et al., 2020; Onojeghuo et al., 2021) This study

VHRS: Very High Spatial Resolution; HSR: High Spatial Resolution; MSR: Moderate Spatial Resolution; UAV: Unmanned Aerial Vehicle; MLC: Maximum Likelihood Classifier; NN: Neural Networks; DT: Decision Tree; SVM: Support Vector Machine; RF: Random Forest.

above 0 °C range from 2000 to 4200 °C·day, and above 10 °C range from 1600 to 3600 °C·day (Dong et al., 2016). Frost-free periods vary between 140 and 170 days (Dong et al., 2016). The average annual precipitation ranges from 500 to 800 mm, most of which occurs in July and August.

Wetlands are a mixture of plants, surface water, and/or watersaturated soil (Mehner, 2009), which are diverse and can be grouped by plant growth form (grass, shrub, tree), life cycle (annual, perennial), leaf seasonality (evergreen, deciduous), and canopy type (open, closed) (Mao et al., 2020; Mehner, 2009; Wang et al., 2020d) (Table 2). Classification of wetlands based on morphological and phenological characteristics will contribute to more accurate estimates of ecological and environmental processes and ensure responsible conservation and development to maximize ecological benefits. Plant growth forms and their life cycle can influence the amount of carbon sequestered (Krauss et al., 2021). It is also possible to identify and assess wetland habitats by classifying and describing wetland vegetation, as wetlands with different plant growth forms and canopy types can indicate the presence of specific flora and fauna adapted to those conditions (Beedy, 1981; Panda et al., 2021; Tanalgo et al., 2015). In addition, such classification has the potential to help in evaluating their ability to filter pollutants and excess nutrients as wetland vegetation type and its growth form can impact its filtering capacity (Boto and Patrick Jr., 1979; Sandoval et al., 2019). In this study we focused on grass wetland with perennial deciduous grass and open canopy (seasonal open-canopy marsh), grass wetland with perennial deciduous grass and closed canopy (yearlong closed-canopy marsh), and forest wetland with perennial deciduous tree and open canopy (deciduous forest swamp) (Fig. 1).

2.2. Datasets

2.2.1. ALOS PALSAR-2 data

We collected 25 m ALOS PALSAR-2 L-band (23.5 cm) imagery for 2020 and 2019 in GEE (Supplementary Fig. 2a). The released yearly PALSAR-2 composite data were mosaic of strip data with minimal response to surface moisture (Shimada et al., 2014), which were ortho-rectified and slope-corrected using the 90 m SRTM digital elevation model (DEM). The PALSAR-2 data comprised two polarizations (HH and HV). The digital numbers (DN) values in the two polarization bands were converted to gamma naught (γ^0) values in decibel unit (dB) using $\gamma^0 = 10log_{10}(DN^2) - 83$ dB (Shimada et al., 2014). We calculated the Ratio (HH/HV) and Difference (HH-HV) values. Approximately 5.5 \times 10⁷ pixels (1.9% of the total pixels) in Northeast China had no PALSAR-2 data in 2020, and they were filled using 2019 PALSAR-2 data (Supplementary Fig. 2a). To avoid the impact of snow and ice, we replaced observations outside of the 2020 growing season with good-quality (no snow and/or ice) data acquired during the 2019 growing season (April to September) (Supplementary Fig. 2b, c). The PLASAR-2 images were resampled to 10 m using the nearest neighbor method to be spatially consistent with the Sentine-1/2 images.

2.2.2. Sentinel-1 data

The C-band (\sim 5.5 cm) Sentinel-1A/B Level 1 Ground Range Detected (GRD) product in the Interferometric Wide (IW) swath model from January 1, 2020, to December 31, 2020, was collected in GEE

(Supplementary Fig. 2d). Sentinel-1 imagery offers dual-polarization with VV and VH bands (Torres et al., 2012). Sentinel-1 data in GEE were pre-processed with the Sentinel-1 Toolbox using orbit metadata update, GRD border noise removal, thermal noise removal, radiometric calibration, and terrain correction. The final terrain-corrected values were converted to dB via 10log10(DN).

2.2.3. Sentinel-2 data

We used all available Sentinel-2A/B Level-2A surface reflectance (SR) data in GEE from January 1, 2020, to December 31, 2020. Good-quality observations were defined as no clouds, cloud shadows, cirrus, and snow/ice. Bad-quality observation with clouds, cloud shadows, and cirrus were identified and removed by using the QA60 bitmask band. Observations with snow/ice were identified and eliminated by using the criteria of nir-infrared (NIR) >0.11 and Normalized Difference Snow Index (NDSI) >0.4 (Zhang et al., 2015).

Normalized Vegetation Index (NDVI) (Tucker, 1979), Enhanced Vegetation Index (EVI) (Huete et al., 1997, 2002), Land Surface Water Index (LSWI) (Xiao et al., 2004, 2005b), and modified Normalized Difference Water Index (mNDWI) (Xu, 2006) were calculated for each image using Eqs. (1)–(4). NDVI and EVI are correlated with vegetation detection and monitoring, LSWI captures vegetation and soil water signals, and mNDWI is commonly used for surface water detection.

$$NDVI = \frac{NIR - Red}{NIR + Red} \tag{1}$$

$$EVI = 2.5 \times \frac{NIR - Red}{NIR + 6Red - 7.5Blue + 1}$$
 (2)

$$LSWI = \frac{NIR - SWIR}{NIR + SWIR}$$
 (3)

$$mNDWI = \frac{Green - SWIR}{Green + SWIR}$$
 (4)

where *Blue, Green, Red, NIR*, and *SWIR* are the SR values of blue (496.6 nm), green (560 nm), red (664.5 nm), near-infrared (835.1 nm), and shortwave-infrared (1613.7 nm) bands for Sentinel-2A MultiSpectral Instrument sensor.

2.2.4. Landsat data

We used Landsat 7/8 Level-2 SR data from January 1, 2020, to December 31, 2020, in GEE. The BQA bitmask band was used to remove clouds, cloud shadows, and cirrus. Snow/ice was removed using the same algorithm described in Section 2.2.3. The spatial distribution of the number and percentage of good-quality observations for Landsat and Sentinel-2 images are presented in Supplementary Fig. 2e, f. NDVI, EVI, LSWI, and mNDWI were calculated for each Landsat image using Eqs. (1)–(4). These vegetation indices collections were resampled to 10 m using the nearest neighbor method.

2.2.5. MODIS land surface temperature data

The night land surface temperature (LST) data from MYD11A2 for 2020, which provide average 8-day data, were used to define the

Table 2Wetland classification system for Northeast China in this study.

Plant growth form	Life cycle	Leaf seasonality and canopy type			
Grass (marsh)	Perennial plants	Deciduous grass, closed canopy	Deciduous grass, open canopy		
Shrub	Perennial plants	Deciduous shrub, closed canopy	Deciduous shrub, open canopy	Evergreen shrub, closed canopy	Evergreen shrub, open canopy
Tree (forest swamp)	Perennial plants	Deciduous tree, closed canopy	Deciduous tree, open canopy	Evergreen tree, closed canopy	Evergreen tree, open canopy

Open canopy - both plant and surface water under the canopy can be directly seen by sensors at least one time in a year; closed canopy - canopy are closed throughout the year and no surface water can be directly seen by sensors throughout the year.

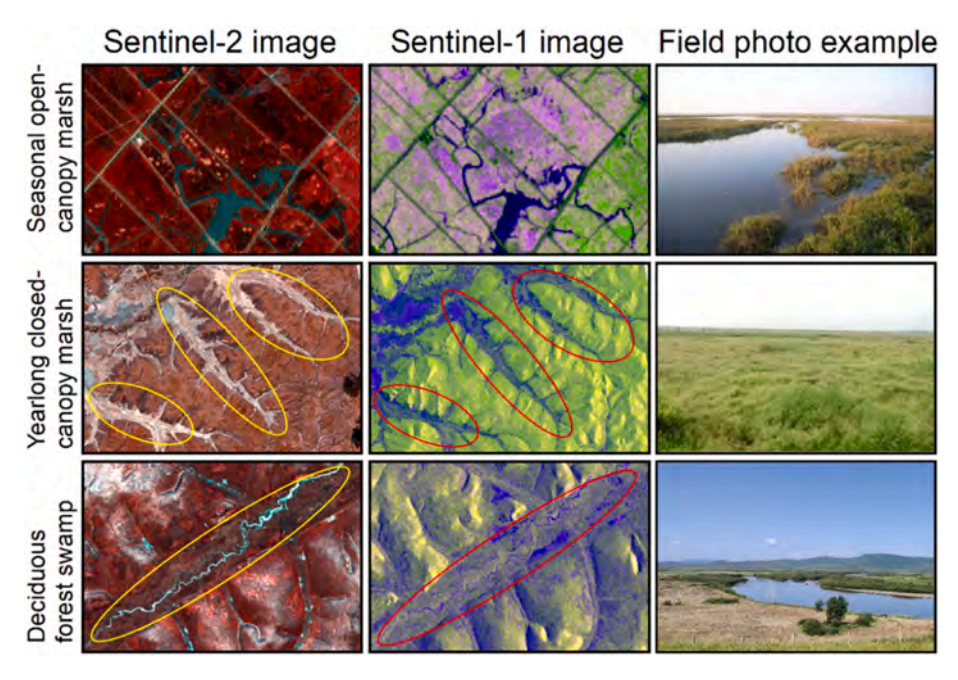


Fig. 1. Satellite images (Sentinel-2 and Sentinel-1) and field photos of seasonal open-canopy marsh, yearlong closed-canopy marsh, and deciduous forest swamp. Field photos of seasonal open-canopy marsh and yearlong closed-canopy marsh were downloaded from the Global Geo-Referenced Field Photo Library (https://www.ceom.ou.edu/photos/). Field photo of deciduous forest swamp was provided by Dr. Chong Huang.

thermal growing season (TGS) by night LST threshold of 0 °C (TGS-0) and 5 °C (TGS-5), i.e., the starting date, ending date, and the duration of night LST above 0 °C and 5 °C (Linderholm et al., 2008) (Supplementary Fig. 3). The non-thermal growing season below 0 °C (NTGS-0) was also identified, i.e., the period from January 1 to the last date of night LST being below 0 °C in spring and from the first date of night LST being below 0 °C in winter until December 31. The digital number (DN) values from MYD11A2 were converted to centigrade unit values using LST (°C) = DN \times 0.02–273.15 (Wan, 2008).

2.2.6. Digital elevation model data

The Shuttle Radar Topography Mission V3 product (SRTM Plus) in GEE is DEM data provided by NASA JPL at a resolution of $\sim\!30$ m (Farr et al., 2007). A slope variable was derived from the DEM data. The DEM and slope maps were resampled to 10 m using the nearest neighbor method.

2.2.7. Ground reference data

Ground reference data include both validation samples for wetland algorithm development and validation samples for available specific land cover mapping algorithms. We used GPS-based field photos, Google Earth VHSR images, and Sentinel-2 images taken circa 2020 to collect ground reference data. First, field photos in Northeast China were collected from the Global Geo-Referenced Field Photo Library (htt ps://www.ceom.ou.edu/photos/). These photos were processed as Keyhole Markup Language (KML) files, referred to as points of interest (POIs), and then geo-linked with Google Earth. Besides the POIs obtained from field photos, we first divided the study area into 122 $1^{\circ} \times 1^{\circ}$ grid cells and randomly generated 5 POIs within each cell. Second, we integrated field photos and Google Earth and Sentinel-2 images as background references to manually digitalized ROIs around the POIs for each land cover type. To ensure accurate sample selection, we considered three Sentinel-2 composites from early April to mid-June, early July to late August, and mid-November to mid-January. POIs with heterogeneous land cover surroundings were excluded. Given the relatively small size of wetlands, we manually selected additional wetland samples. Due to the difficulty of visually distinguishing between seasonal open-canopy marsh and yearlong closed-canopy marsh, we only

collected samples for the broad category of marsh. Marsh with seasonal open-canopy or yearlong closed-canopy will be identified by time series satellite data in the classification process.

In total, we delineated 122 marsh, 49 deciduous forest swamp, 76 paddy rice, 26 grassland, and 76 dryland ROIs (Supplementary Fig. 4a) to evaluate the stability of the unique optical and/or microwave characteristics (knowledge) of wetlands identified in this study, and to set thresholds for wetland mapping algorithms. Additionally, 69 forest, 17 evergreen vegetation, 30 sparse vegetation (saline and alkaline land, built-up and barren land), and 23 surface water ROIs (Supplementary Fig. 4b) were selected to evaluate the applicability of the existing specific land cover mapping algorithms in Northeast China.

2.3. Methods

Fig. 2 illustrates the workflow of the knowledge-based wetland mapping algorithms for Northeast China. First, we identified and masked out several non-wetland types by applying or modifying the available specific land cover mapping algorithms which were developed in our previous studies (Dong et al., 2015; Qin et al., 2015; Wang et al., 2020c, 2020d; Zhang et al., 2015; Zou et al., 2018). Second, we identified and mapped seasonal open-canopy marsh and yearlong closed-canopy marsh among the remaining pixels. Finally, the deciduous forest swamp was delineated within the deciduous forest layer.

2.3.1. Application of available land cover mapping algorithms

In previous studies, we developed knowledge-based algorithms to map specific land cover types with high accuracies, including forest (Qin et al., 2015), evergreen vegetation (Dong et al., 2015; Wang et al., 2020d), yearlong surface water (Wang et al., 2020c; Zou et al., 2018), and sparse vegetation (Zhang et al., 2015). Here we used the same algorithms and time series image data (Fig. 3) in 2020 to generate annual maps of forest, evergreen vegetation, yearlong surface water, and sparse vegetation in Northeast China in 2020. These maps served as masks for wetland identification. Detailed description can be found in (Supplementary Note 1).

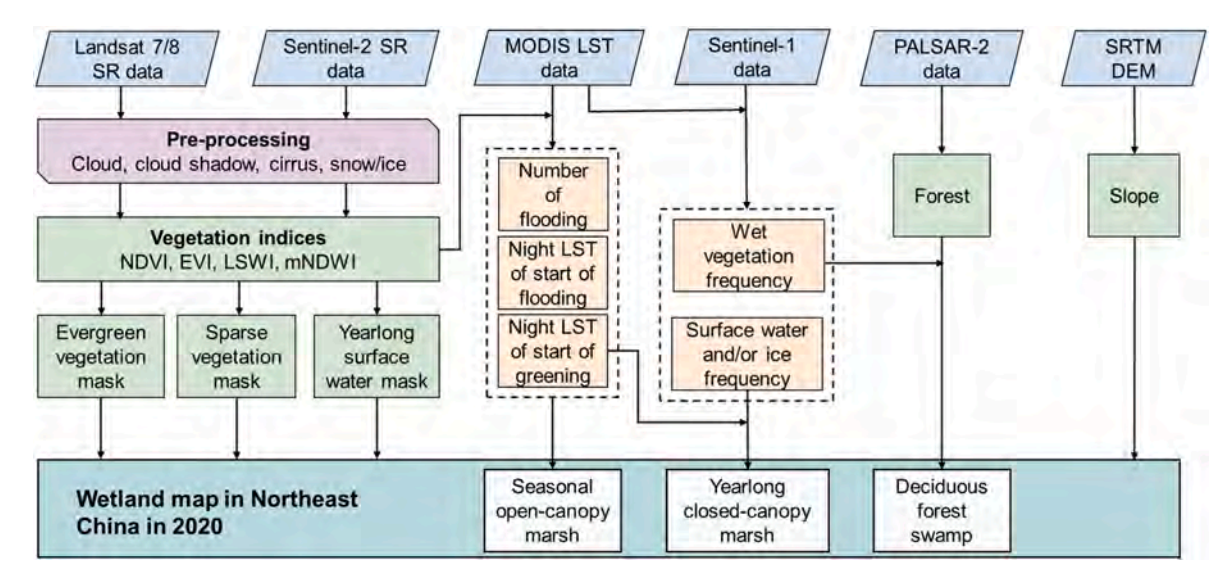


Fig. 2. The flowchart for identifying different types of wetland in Northeast China.

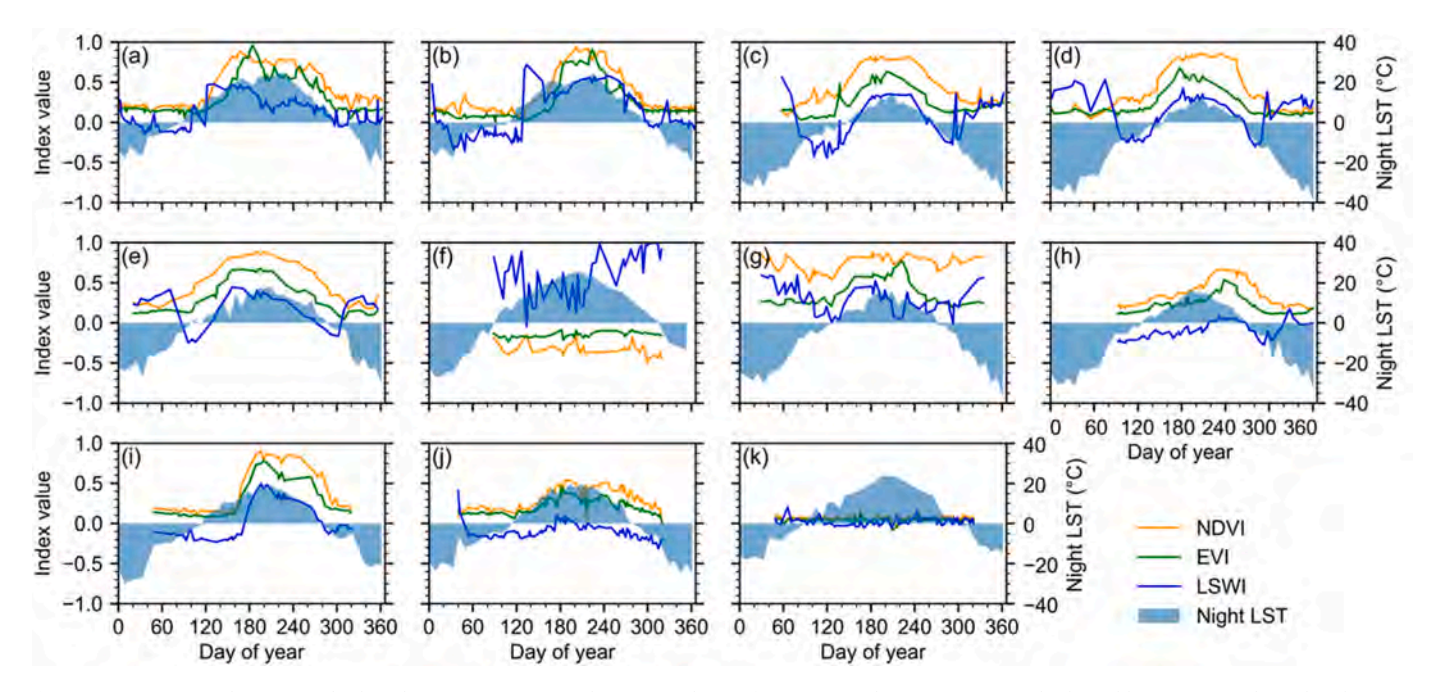


Fig. 3. Time series Landsat/Sentinel-2-based NDVI, EVI, LSWI, and MODIS night LST for (a) seasonal open-canopy marsh, (b) paddy rice, (c) yearlong closed-canopy marsh, (d) deciduous forest swamp, (e) deciduous forest, (f) yearlong surface water body, (g) evergreen forest, (h) upland crop, (i) dryland, (j) saline and alkaline land, and (k) built-up in 2020.

2.3.2. Development of new algorithms for wetlands mapping

2.3.2.1. Algorithm to identify seasonal open-canopy marsh. In the early growing season, when snow/ice melts, seasonal open-canopy marshes are observed as a mix of green plants and water. The open-canopy and flooded (or inundated) marsh fields have a spectral signature of LSWI > EVI or LSWI > NDVI (Fig. 3a), which is interpreted as water-related vegetation index larger than greenness-related vegetation index (Xiao et al., 2002). Paddy rice also has a flood/open-canopy stage in its transplanting phase, leading to confusion between seasonal open canopy marshes and paddy rice (Wang et al., 2020d; Zhou et al., 2016). However, the marshes, one of natural wetlands, have several unique features compared to paddy rice. First, the marshes start to flood after snow/ice starts to melt and temperature rises above 0 °C in early spring (Fig. 3a), whereas rice fields are not irrigated or flooded until a specific

temperature threshold is reached in late spring (Fig. 3b). Second, the marshes start to green up when air temperature is above 0 °C in early spring (Fig. 3a), while rice transplanting occurs in late spring, when a stable air temperature threshold is reached to avoid the cold temperature damage to rice seedlings (Fig. 3b). By late May, the marshes have already developed into a closed canopy while paddy rice field is still in the flooding stage (Dong et al., 2016; Mao et al., 2020). In other words, the marshes green up much earlier than do paddy rice. Third, the flooding period of the marshes is shorter compared to paddy rice. Flooding signals in rice fields can persist for approximately 2 months–80 days after transplanting until the rice canopy becomes closed (Dong et al., 2016; Xiao et al., 2005a).

To examine the generalizability of phenological distinctions between seasonal open-canopy marshes and paddy rice, we analyzed three phenological metrics: night LST of start of flooding (nLST_{SOF}), night LST

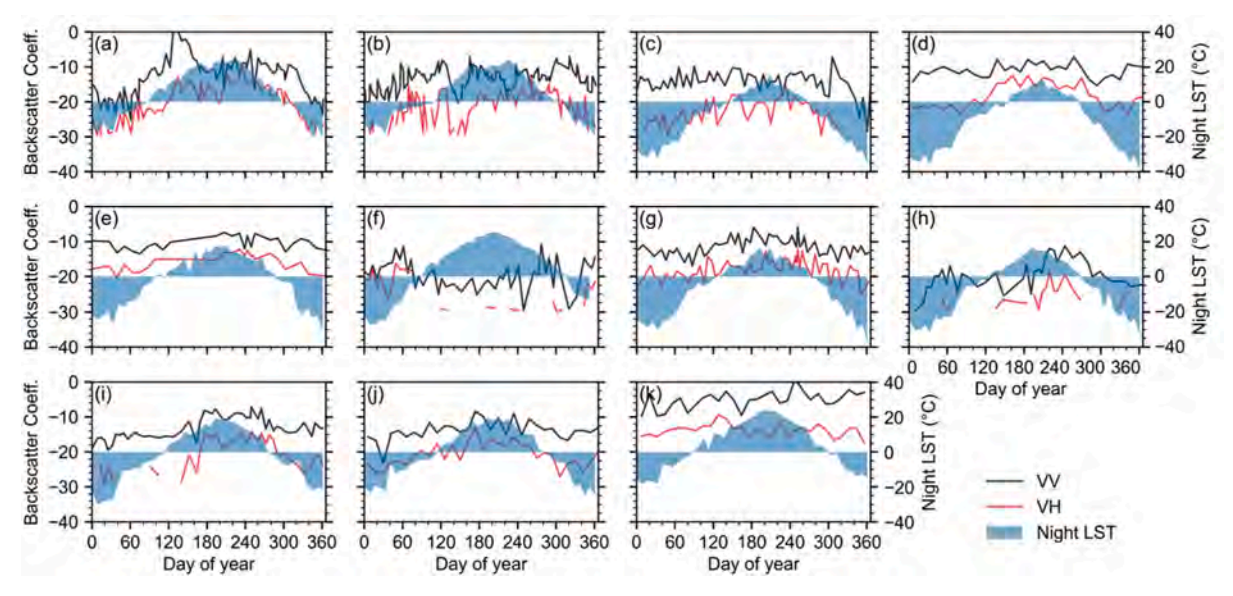


Fig. 4. Time series Sentinel-1 VV, VH, and MODIS night LST for (a) seasonal open-canopy marsh, (b) paddy rice, (c) yearlong closed-canopy marsh, (d) deciduous forest swamp, (e) deciduous forest, (f) yearlong surface water body, (g) evergreen forest, (h) grassland, (i) upland crop, (j) saline and alkaline land, and (k) built-up in 2020.

of start of greening (nLST_{SOG}), number of floodings (NF) between the starting of night LST over 0 $^{\circ}$ C (TGS-0-S) and the end of June (DOY = 181). Using the NF layer to overlay marsh samples, we categorized marsh pixels that had at least one flooding signature as seasonal opencanopy marshes. The remaining pixels were labeled as yearlong closed-canopy marshes and were used for knowledge validation and mapping algorithm development for yearlong closed-canopy marshes. Then we overlaid paddy rice and seasonal open-canopy marsh samples with these three phenological metrics and evaluated their separability (Fig. 5a-c). The histograms showed that most seasonal open-canopy marsh pixels had NF of ≥ 1 (Fig. 5a), nLST_{SOF} of 0 °C-12 °C (Fig. 5b), and nLST_{SOG} of 0 °C-13 °C (Fig. 5c). While most paddy rice pixels had NF of \geq 2 (Fig. 5a), nLST_{SOF} of \geq 5 °C (Fig. 5b), and nLST_{SOG} of \geq 10 °C (Fig. 5c). These unique phenological characteristics of seasonal opencanopy marsh are consistent with the knowledge obtained from the time series profile and phenological analysis (Fig. 3a and b). Therefore, we removed the paddy rice from flooded pixels using (NF >2, nLST_{SOF} >5 °C, and nLST_{SOG} >10 °C). The remaining flooded pixels were used as baseline map for the seasonal open-canopy marsh identification.

Slope and elevation were considered to exclude areas with high elevation and/or steep slope where wetlands are unlikely to occur. Most marsh and forest swamp sample pixels had slopes $<6^{\circ}$ (Supplementary Fig. 5a). Elevation, however, did not have a clear distributional pattern (Supplementary Fig. 5b). Thus slope $<6^{\circ}$ was used as a supplementary criterion to limit wetland boundaries. In summary, seasonal opencanopy marsh was delineated using Eq. (5).

Seasonal open — canopy marsh = NF
$$\geq$$
 1, $~0~^{\circ}C \leq nLST_{SOF} \leq$ 12 $^{\circ}C,~0~^{\circ}C$
$$\leq nLST_{SOF} \leq 13~^{\circ}C,~and~Slope~<6^{\circ} \eqno(5)$$

2.3.2.2. Algorithm to identify yearlong closed-canopy marsh. Yearlong closed-canopy marsh lacks a distinct spectral "flooding" signal due to the inability of optical sensors to detect surface water beneath the canopy. However, it still exhibits distinguishable microwave signals compared to non-flooded (or upland) vegetation due to the surface water or water-supersaturated soil under the canopy. Sentinel-1 is sensitive to moisture, capable of penetrating less dense vegetation and interacting with its structure, and has been successfully applied to monitor changes in vegetation and soil moisture (Geudtner et al., 2014). As illustrated in

Fig. 4c, during TGS-0 period, yearlong closed-canopy marshes had a unique feature of -16 < VV < -10. In comparison, grasslands had VV < -16 (Fig. 4h), and upland crops had VV > -10 (Fig. 4i). Furthermore, marsh plants exhibit earlier greening compared to upland crops (Fig. 3c, i), as upland crops in Northeast China are typically sown after average daily temperatures stabilize above 10 °C (Chu and Guo, 2018).

We calculated the median values of VV during TGS-0 period, and the histograms suggested that $-16 < \mathrm{VV} < -10$ could discriminate yearlong closed-canopy marshes from upland vegetation (grassland and upland crop) (Fig. 5d), which is consistent with the knowledge for yearlong closed-canopy marsh discovered in the time series for individual pixels (Fig. 4c, h, i). Thus, we used $-16 < \mathrm{VV} < -10$ to identify wet vegetation in yearlong closed-canopy marshes. The wet vegetation frequency in TGS-0 (WVF $_{\text{TGS-0}}$) was calculated as the ratio of the wet vegetation observations to the Sentienl-1 observations in TGS-0, to maximize the benefit of time series images and reduce errors induced by noise. Most yearlong closed-canopy marshes had WVF $_{\text{TGS-0}} \ge 0.50$ (Fig. 5e) and nLST $_{\text{SOG}}$ of 2 °C–13 °C (Fig. 5f). Combining the analysis of slope (Supplementary Fig. 5a), the algorithm for identifying yearlong closed-canopy marsh was developed using Eq. (6).

Yearlong closed — canopy marsh = WVF
$$_{TGS-0} \ge 0.50,~2~^{\circ}C \le nLST_{SOF}$$
 $\le 13~^{\circ}C,~and~Slope~< 6^{\circ}$ (6)

2.3.2.3. Algorithm to identify deciduous forest swamp. Although L-band PALSAR-2 is highly penetrating, the released yearly PALSAR data are mosaic of strip data with minimal response to surface moisture and is mostly concentrated in the growing season, making it difficult to detect surface water under the forest canopy. Dense time series Sentinel-1 images have the potential to monitor the dynamic of the wetland moisture in a year. C-band Sentinel-1 backscatters reflect the top of the tree canopy (Geudtner et al., 2014), but for sparse forests, especially in leaf-off conditions, it can still interact with the surface water and/or ice on the ground (Martinis and Rieke, 2015). As depicted in Fig. 4, in NTGS-0 period, the seasonal dynamics of VH of deciduous forest swamp differed from those of deciduous forest: deciduous forest swamp had lower VH values (<-20) caused by the surface water and/or ice under the canopy (Fig. 4d), while the deciduous forest kept higher VH values (>-20) for most of the period (Fig. 4e).

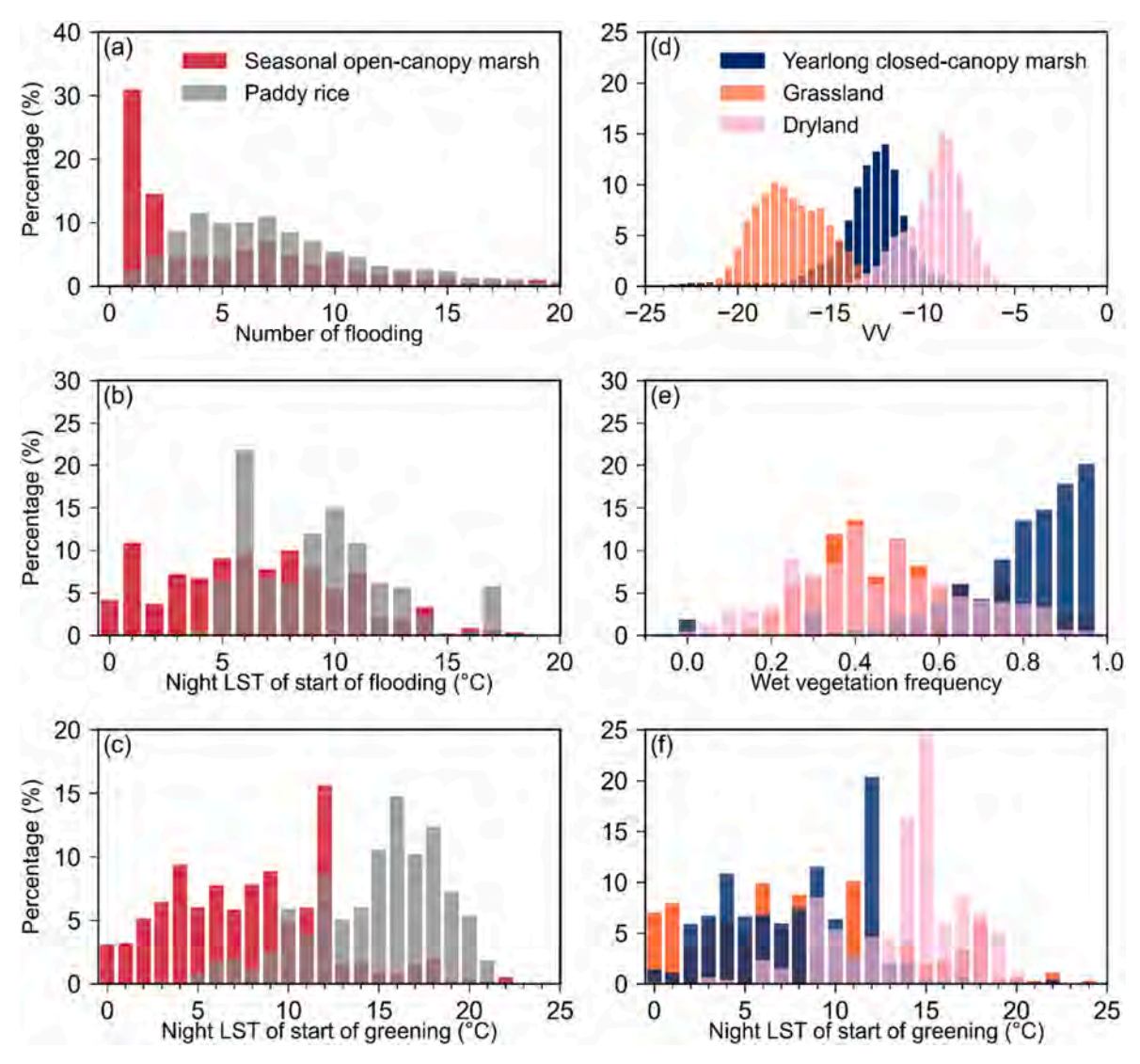


Fig. 5. Index distributions of seasonal open-canopy marsh (a–c) and yearlong closed-canopy marsh (d–f). (a)–(c), Signature analysis of seasonal open-canopy marsh and paddy rice at (a) number of flooding, (b) night land surface temperature (LST) of start of flooding, and (c) night LST of start of greening. (d–f), Signature analysis of yearlong closed-canopy marsh and upland vegetation (grassland and dryland) at (d) VV values, (e) wet vegetation frequency, and (f) night LST of start of greening.

We calculated the median VH values during NTGS-0 period, and the histograms showed that VH $<\!-20$ could distinguish deciduous forest swamps from deciduous forests (Fig. 6a), which is consistent with the knowledge obtained from the time series of individual pixels illustrated in Fig. 4d and e. Hence, we used VH $<\!-20$ to identify surface water and/

or ice in the NTGS-0 period (Fig. 6a). Surface water and/or ice frequency in the NTGS-0 period (SWIF_{NTGS-0}) was calculated as the ratio of surface water and/or ice observations to Sentinel-1 observations in NTGS-0. Notably, most of forest swamps had SWIF_{NTGS} \geq 0.40 (Fig. 6b). Due to the overlapping of SWIF_{NTGS-0} between deciduous forest swamps and

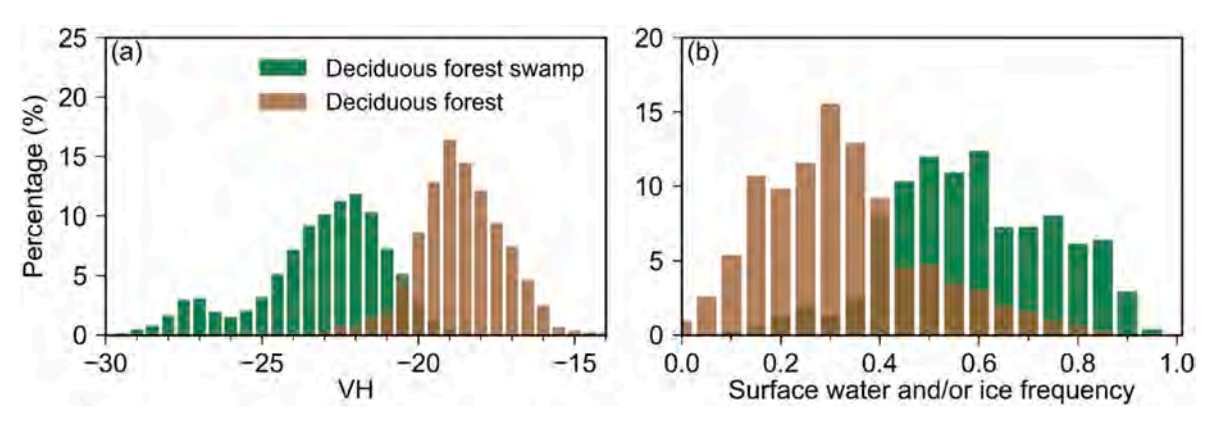


Fig. 6. Index distributions of deciduous forest swamp and deciduous forest at (a) VH values and (b) surface water and/or ice frequency.

deciduous forests, we applied a relatively strict threshold (SWIF $_{\rm NTGS}$ \geq 0.45) for deciduous forest swamp to avoid confusion with deciduous forest. Finally, the algorithm described in Eq. (7) was implemented to distinguish deciduous forest swamp from deciduous forest layer.

Deciduous forest swamp =
$$SWIF_{NTGS-0} \ge 0.45$$
 and slope $< 6^{\circ}$ (7)

2.4. Validation of wetland map for Northeast China in 2020

To develop the validation dataset, we first divided the study area into $122\ 1^\circ \times 1^\circ$ grid cells. Ten random points and square buffers with 60 m by 60 m were generated in each grid cell. Each buffer was visually checked with VHSR images in Google Earth and Sentinel-2 images in 2020. We only collected validation samples of the broad category of marshes due to the difficulty of identifying seasonal open-canopy marsh and yearlong closed-canopy marsh by visual interpretation. Finally, 144 polygons (31,252 pixels) for marsh, 60 polygons (12,815 pixels) for deciduous forest swamp, and 958 polygons (161,253 pixels) for non-wetland were collected (Supplementary Fig. 4c) to generate a confusion matrix to evaluate our resultant wetland map.

2.5. Comparison with other wetland datasets

We collected three wetland datasets to assess the consistency and differences with the results in this study. Mao et al. (2020) produced a nationwide wetland map (CAS_Wetlands) by analyzing Landsat 8 images circa 2015, using a hybrid object-based and hierarchical classification approach. We merged inland marsh and coastal marsh in the CAS_Wetlands as marsh, inland swamp and coastal swamp as swamp for comparison with our marsh and swamp data.

Zhang et al. (2023b) generated a global 30 m wetland map for 2020 (GWL_FCS30) by integrating various wetland data products, time-series satellite images from Landsat and Sentinel-1, and a stratified classification strategy. We merged marsh and salt marsh in the GWL_FCS30 into marsh, swamp and mangrove into swamp.

The third national land survey (NLS3) of China used satellite images with finer than 1 m spatial resolution as the base maps to generate land cover maps and calculate their areas in 2019–2021. We used the NLS3 data in 2020 to do the area comparison with our wetland datasets. Wetlands in NLS3 include seven secondary categories: mangrove, forest swamp, shrub swamp, marsh meadow, inland mudflats, coastal mudflats, and marshland. We summed the areas of marsh meadow and marshland as marsh area, and the areas of mangrove, forest swamp, and shrub swamp as swamp area.

3. Results

3.1. Accuracy assessment for the wetland map in 2020

The confusion matrix showed a good consistency between the mapped pixels and the ground reference pixels in our wetland map for Northeast China in 2020, with an overall accuracy (OA) and Kappa

Table 3 Confusion matrix for the wetlands map in 2020.

Classification	Ground references			Total	UA
	Marsh	Deciduous forest swamp	Non- wetland		
Marsh	28,319	511	2595	31,425	0.90
Deciduous forest swamp	589	10,921	1755	13,265	0.82
Non-wetland	2344	1383	193,808	197,535	0.98
Total	31,252	12,815	198,158	242,225	OA = 0.96
PA	0.90	0.85	0.98		Kappa = 0.88

coefficient of 0.96 and 0.88, respectively (Table 3). The accuracy of the marsh category showed high accuracy with a producer's accuracy (PA) and user's accuracy (UA) both at 0.90. Deciduous forest swamp had a slightly lower accuracy with a PA of 0.85 and a UA of 0.82, respectively, primarily due to the confusion between some of the deciduous forest swamp pixels and non-wetlands (mainly deciduous forest).

3.2. Spatial and area distribution of wetlands in 2020 over Northeast China

In 2020, there were a total of 154,254 km² of wetlands, covering 12.4% of the land area of Northeast China (Fig. 7, Table 4). Out of the total wetland area in 2020, 17.7% were seasonal open-canopy marshes, 44.8% yearlong closed-canopy marshes, and 37.5% deciduous forest swamps. Seasonal open-canopy marsh was mainly found along rivers in plains and estuaries with gentle terrain (i.e., Sanjiang Plain, Songnen Plain, and Liaohe Plain) (Fig. 7). Yearlong closed-canopy marsh was predominantly observed in western and northwestern region of Northeast China with higher elevations (e.g., Hulunbuir Grasslands and Greater Khingan Mountains). Deciduous forest swamp was mainly distributed along the rivers in the mountainous areas with gentle slopes, such as Greater and Lesser Hinggan Mountains.

Among the provinces in Northeast China, Heilongjiang had the most extensive wetland coverage, followed by Inner Mongolia, Jilin, and Liaoning. Marsh (seasonal open-canopy marsh and yearlong closed-canopy marsh) was primarily concentrated in Heilongjiang and Inner Mongolia Provinces. Specifically, Heilongjiang Province had the largest areas of seasonal open-canopy marsh and deciduous forest swamp, while Inner Mongolia Province had the largest extent of yearlong closed-canopy marsh.

3.3. Inter-comparison with wetland datasets

We compared the estimated wetland areas of this study and compared them to CAS_Wetlands, GWL_FCS30, and NLS3 datasets (Fig. 8). The total marsh area in the Northeast China from our study was 96,376 km², which was 37.1% larger than that from the CAS_Wetlands (70,272 km²), 627.5% larger than that from GWL_FCS30 (13,248 km²), and 173.0% larger than that from the NLS3 (35,297 km²). At the municipal scale, our marsh areas matched well with the area of CAS_Wetlands with a slope of 0.89 and R^2 of 0.94 (Fig. 8c), while the agreements between our marsh datasets and GWL_FCS30, and NLS3 were relatively low. In particular, we detected much more marshes (33,207 km²) than GWL_FCS30 (1988 km²) and NLS3 (14,964 km²) in Hulunbuir City (Figs. 8c and 9). The vast majority of marshes in Hulunbuir City were not identified by GWL FCS30 (Fig. 9a4, b4, c4).

Our dataset has a total of 57,877 km² of deciduous forest swamp in the Northeast China, which was 780.0% larger than that from the CAS_Wetlands (6577 km²), 3273.9% larger than that from GWL_FCS30 (1715 km²), and 126.5% larger than that from the NLS3 (25,551 km²). The consistency of our deciduous forest swamps is high with NLS3 and low with CAS_Wetlands and GWL_FCS30 at the municipal level (Fig. 8d). In Hulunbuir City, we detected much more swamps (18,482 km²) than the CAS_Wetlands (641 km²), GWL_FCS30 (271 km²), and NLS3 (8827 km²) datasets (Figs. 8d and 9). A large percentage of swamp pixels in CAS_Wetlands in Hulunbuir City were merged into surrounding marsh patches due to the object-based approach used in CAS_Wetlands (Fig. 9a3, b3, c3). GWL_FCS30 did not identify the vast majority of swamps in Hulunbuir City (Fig. 9a4, b4, c4).

4. Discussion

4.1. Knowledge-based mapping algorithms for marshes

The confusion between seasonal open-canopy marsh and paddy rice has been a major challenge in both paddy rice mapping (Son et al., 2014;

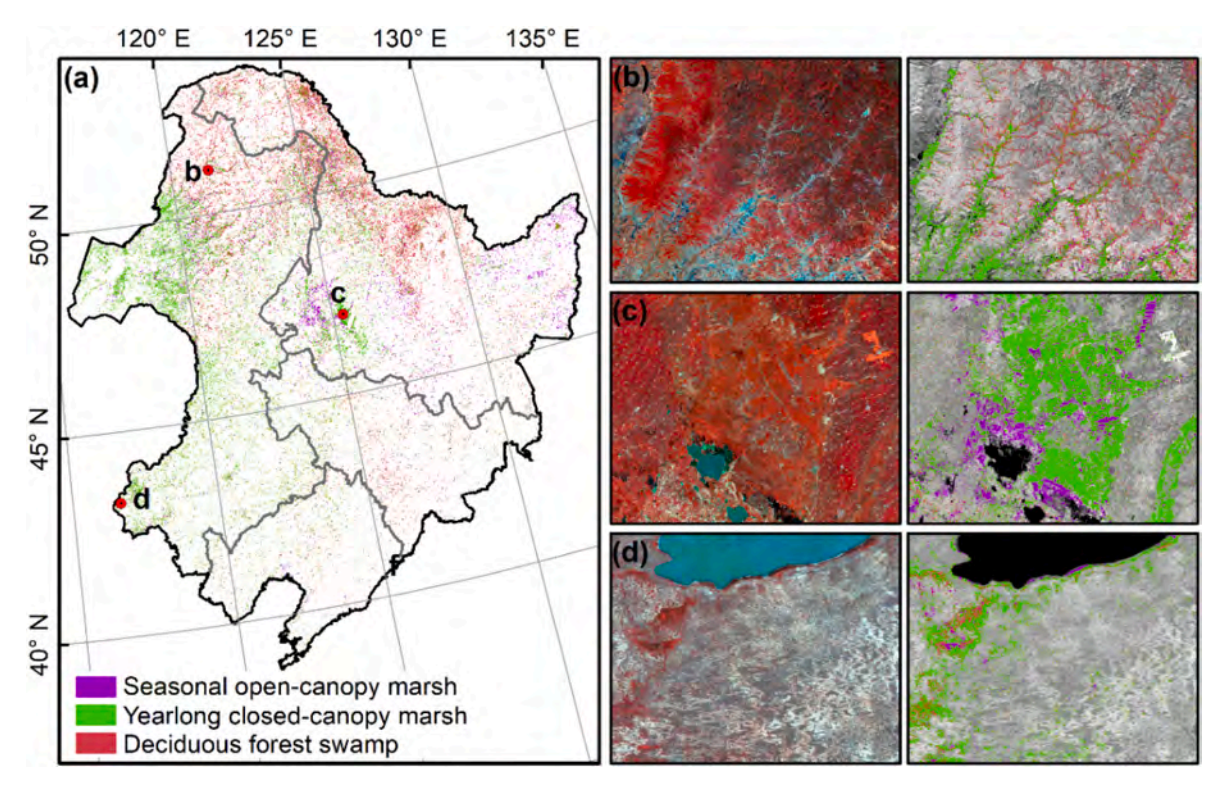


Fig. 7. (a) Spatial distribution of wetlands in Northeast China in 2020. (b-d), Zoom-in views of typical regions and corresponding Sentinel-2 images.

Table 4 Wetland areas (km^2) and percent of corresponding provinces and Northeast China in 2020.

Province	Seasonal	Yearlong	Deciduous	Marsh	Wetland
	open-	closed-	forest		
	canopy	canopy	swamp		
	marsh	marsh			
Heilongjiang*	18,087	19,280	31,065	37,367	68,432
	(4.0%)	(4.3%)	(6.9%)	(8.3%)	(15.1%)
Jilin*	1543	3874	3862	5417	9279
	(0.8%)	(2.0%)	(2.0%)	(2.8%)	(4.9%)
Liaoning*	849	3367	1937	4215	6152
	(0.6%)	(2.3%)	(1.3%)	(2.9%)	(4.2%)
Inner	6740	42,637	21,014	49,377	70,391
Mongolia*	(1.5%)	(9.4%)	(4.6%)	(10.9%)	(15.5%)
Total**	27,219	69,158	57,878	96,376	154,254
	(2.2%)	(5.6%)	(4.7%)	(7.8%)	(12.4%)

Marsh = seasonal open-canopy marsh + yearlong closed-canopy marsh. Wetland = marsh + deciduous forest swamp. * Percent of corresponding province; ** Percent of land area of Northeast China.

Xiao et al., 2005a; Zhang et al., 2015) and marsh mapping (Mao et al., 2020), due to their similar spectral or backscatter signals of inundation or flooding. In this study, we developed a knowledge-based seasonal open-canopy marsh mapping algorithm by analyzing time series Landsat/Sentinel-2 images. Seasonal open-canopy marsh and paddy rice differed notably in the three unique phenological metrics (NF, nLST_{SOF}, and nLST_{SOG}) designed in this study. NF and nLST_{SOF} can characterize the differences between seasonal open-canopy marsh and paddy rice in terms of flooding, while nLST_{SOG} not only captures their distinctions in terms of greening but also ensures that the identified pixels contain green vegetation, effectively eliminating the influence of non-vegetated flooded areas due to snow and ice melting and short-term heavy rainfall. In addition, our study used all available optical data (Landsat and Sentinel-2) to increase the numbers of good-quality observations for seasonal open-canopy marsh mapping algorithm. Compared to the previous studies using only Landsat (Mao et al., 2020; Zhang et al.,

2023b), the combination of Landsat and Sentinel-2 substantially increased the number of good-quality observations in a single year, allowing us to better track the phenology of natural marshland and paddy rice at a higher spatial resolution (10 m) and a shorter temporal resolution (<5 days).

The knowledge-based yearlong closed-canopy marsh mapping algorithm developed in this study demonstrated the potential of combing time series Sentinel-2/Landsat and Sentinel-1 images for identifying yearlong closed-canopy marshes accurately. Notably, we identified a distinct VV value range for wet vegetation due to the higher soil moisture content of yearlong closed-canopy marshes, especially during the thermal growing season over 0 °C. The resulting wet vegetation frequency, together with $nLST_{SOG}$, can effectively separate yearlong closed-canopy marshes from upland vegetation. Several studies have also emphasized the significance of utilizing Sentinel-1 VV and VH polarization bands in mapping both coastal and inland wetlands (Hu et al., 2021; Zhang and Lin, 2022). Some studies have incorporated the difference, sum, normalized difference, and sum of squares of VV and VH bands into wetland mapping approaches (Hemati et al., 2023; Hu et al., 2021), so we can also investigate the use of these metrics in the future work.

4.2. Comparison of deciduous forest swamp maps

Comparison of our deciduous swamp map with the other datasets showed some differences among these datasets in area estimates (Fig. 8b, d) and spatial distribution (Fig. 9). The input image data from different years and forest swamp mapping algorithms contributed to the inconsistency between our deciduous forest swamp map and CAS_Wetlands. The CAS_Wetlands used Landsat 8 images acquired at peak growing season (July to August) circa 2015 (Mao et al., 2020). Forests in the peak growing season have closed canopies, and thus forest swamps are unavoidably difficult to distinguish from unflooded forest and other vegetation types that have similar spectral characteristics. In our study, we first identified deciduous forest using PALSAR-2 and time series Landsat/Sentinel-2 data, and then used surface water and/or ice

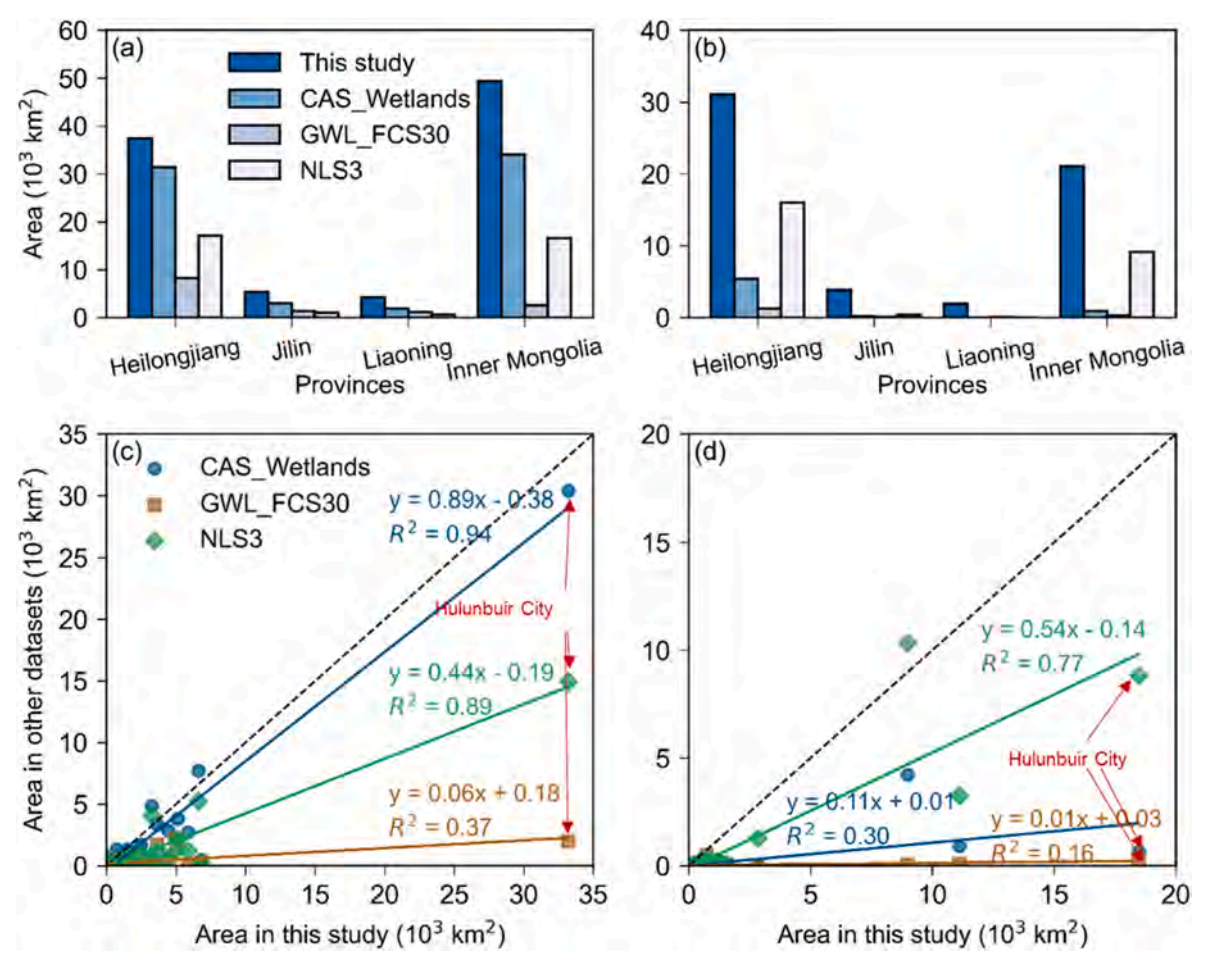
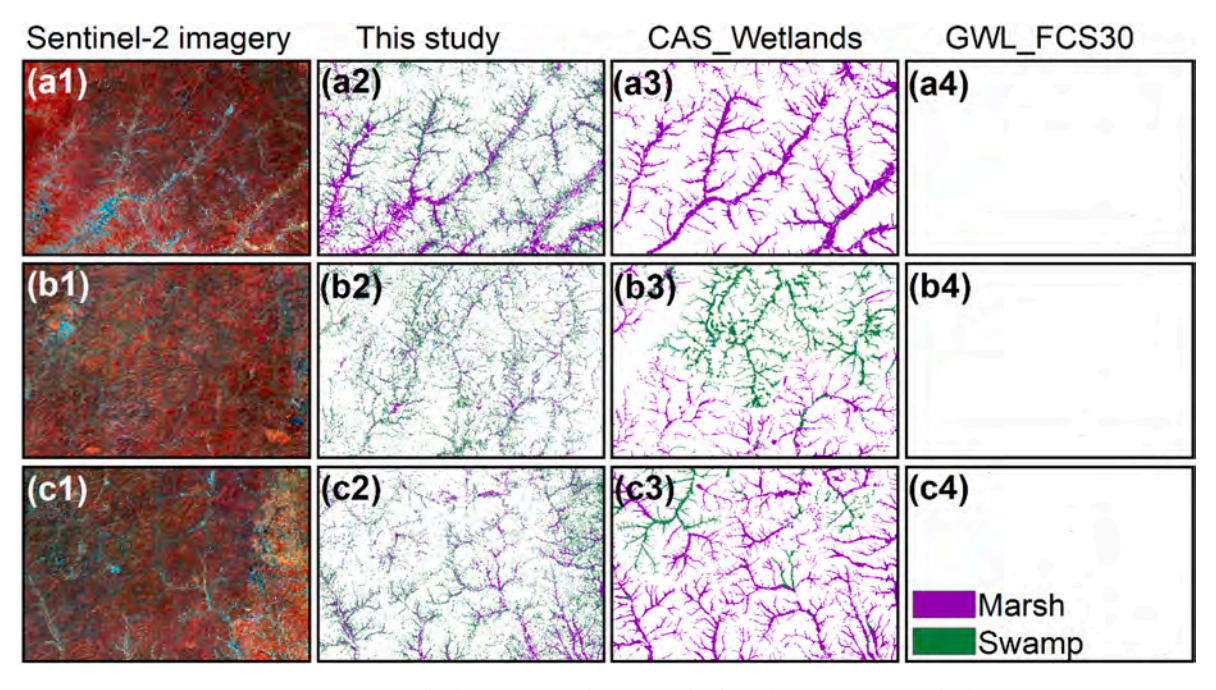


Fig. 8. The comparison of wetland areas estimated by this study and other datasets. (a)–(b), Comparison of (a) marsh and (b) deciduous forest swamp areas at provincial level. (c)–(d), Comparison of (c) marsh and (d) deciduous forest swamp areas at municipal level using the linear regression method.



 $\textbf{Fig. 9.} \ \ \textbf{Zoom-in views of wetlands from our study, CAS_Wetlands, and GWL_FCS30 in Hulunbuir City.}$

frequency derived from time series Sentinel-1 data to identify forest swamps from the deciduous forest layer. By identifying deciduous forests first largely reduced the confusion between woody swamps and herbaceous marshes. Moreover, the use of entire-year time series data better captured the phenological information of various land cover types. In the leaf-off phase of deciduous forests, Sentinel-1 images show the information of surface water and/or ice under the canopy. The 10 m spatial resolution of our forest swamp map and the 30 m of CAS Wetlands dataset also contributed to the area differences. Forest swamps mainly form along streams in valleys in Northeast China, where limited water level fluctuations due to rainfall and seasonal flooding lead to fragmented and complex swamps with widths less than 30 m, observed through visual and manual measurements on Google Earth. The 30 m resolution in CAS Wetlands may result in mixed pixel phenomena, detecting forest swamps only if they cover a significant portion of the pixel size (30 m), affecting the spectral signal. In contrast, our study with finer 10 m Sentinel-1 images can reduce mixed pixels and thus identify forest swamps more accurately (Fig. 9a-c).

In mapping algorithms, we used pixel- and knowledge-based approach to detect deciduous swamps, while CAS Wetlands map used object-based image analysis (Mao et al., 2020). The smoothing effect of object-based analysis tends to assign mixed Landsat pixels containing forest swamps to surrounding non-swamp categories, causing an underestimation of forest swamp area (Fig. 9). Moreover, CAS_Wetlands map set a single segmentation scale for each path/row, which may not adequately represent the properties of real objects of the fragmented and complex wetland landscapes within such large areas of a Landsat path/row (approximately 182 km × 185 km) (Song et al., 2005). Some empirical values were used in the segmentation and classification rules in CAS_Wetlands classification process due to limited field samples, which might also introduce uncertainties. In contrast, our pixel- and knowledge-based algorithm analyzed the spectral and structural information of individual pixels over time, effectively avoiding the influence of surrounding pixels on forest swamp identification.

Several factors may contribute to the inconsistency between our deciduous forest swamp map and GWL_FCS30 (Fig. 8b, d, Fig. 9). First, GWL_FCS30 initially determined the maximum wetland extents by combining multiple prior wetland data products. Any pixels classified as a forest swamp outside the maximum extent were identified as a misclassification. This scheme might overlook areas with actual forest swamps, leading to an underestimation of the true extent. Second, GWL_FCS30 used random forest method to identify wetlands, and we used knowledge-based algorithm. Third, the different spatial resolutions between our swamp map (10 m) and GWL_FCS30 (30 m) also contribute to the forest swamp area differences.

4.3. Potential sources of error in the wetlands map

The accuracy of the wetlands map can be affected by various factors, including image data, training data, algorithms, and land cover classification scheme and definition. Some bad-quality observations in Landsat and Sentinel-2 imagery may remain after quality filtering due to the quality of QA band (Zhu and Woodcock, 2012; Zou et al., 2018), which might introduce low-frequency flooding noise over non-wetland pixels, leading to uncertainties in the resultant maps. Although we maximized the number of observations by combining all available Landsat 7/8 and Sentinel-2, some pixels may still have a limited number of good-quality observations between the start date of 0 °C and the end of June, and thus may not detect flooding signals in seasonal open-canopy marshes.

Limited *in-situ* (ground) reference data and visual interpretation and delineation of the regions of interest (ROIs) may introduce errors into the classification process and accuracy assessment. In particular, few field photos and *in-situ* data were available for wetlands in the Greater Khingan Mountains area due to its less accessible nature and the complex boundaries of wetland landscape. To reduce such uncertainties,

extensive efforts were devoted to generating numerous random polygons to assess wetland maps for 2020. Historical datasets like China's wetland map can be important reference data for future effort (Mao et al., 2020). Additionally, marsh samples were not divided into seasonal open-canopy marsh and yearlong closed-canopy marsh for validation in this study, as there were no field samples available for either category since people often conduct field surveys during the peak growing season when the canopy is closed, and the human eye can hardly distinguish these two categories from images. Our study demonstrated that the time-series remote sensing method has the capacity to distinguish these two types of marshes, but there is still a need to increase the number of field observations to verify the classification methods.

The seasonal dynamics of natural wetlands are relatively consistent in normal years, and thus the knowledge-based mapping algorithm can be applied in other years. However, extreme climate events such as flooding events during the flooding/transplanting period, may affect NF of paddy rice and natural wetlands. When applying these mapping algorithms to other regions with different climates and agricultural practice, careful study of NF of paddy rice and natural wetlands in the study regions would be helpful and should be carried out. Additionally, irrigation or flooding events in non-water related land cover types during the flooding period of wetlands might introduce uncertainties to the annual maps of seasonal open-canopy marshes.

5. Conclusions

Accurate and up-to-date large-scale annual maps of wetlands, including seasonal open-canopy marsh, yearlong closed-canopy marsh, and deciduous forest swamp, have been very limited in China. We proposed and applied knowledge-based algorithms to map wetlands in Northeast China at 10 m spatial resolution by using all available L-band PALSAR-2, C-band Sentinel-1, Landsat, Sentinel-2, and MODIS land surface temperature images in 2020. Optical images can be used to identify those grass wetlands with open canopies. C-band SAR images can be used to identify marshes with closed canopies. A combination of C-band and L-band SAR images can be used to identify those wetlands dominated by woody plants with open canopies. The Kappa, overall, producer's, and user's accuracies indicated that our resultant wetland map were reasonably accurate. The knowledge-based wetland mapping algorithms highlight the potential for identifying and mapping wetlands at annual scales over large spatial domain using multiple sources of remote sensing data. Such classification considers the capacity of remote sensing technology, which is a viable way to characterize wetlands. Our resultant wetland maps could provide essential information for policy development and wetland conservation and management in the Northeast China.

Credit author statement

Chenchen Zhang: Conceptualization, Methodology, Software, Formal analysis, Validation, Visualization, Writing - original draft, Writing -review & editing. Xiangming Xiao: Conceptualization, Methodology, Writing - review & editing, Supervision, Project administration, Funding acquisition. Xinxin Wang: Methodology, Writing - Review & Editing. Yuanwei Qin: Methodology, Writing - Review & Editing. Russell Doughty: Writing - Review & Editing. Xuebin Yang: Writing - Review & Editing. Yuan Yao: Software, Writing - Review & Editing. Jinwei Dong: Writing - review & editing.

Declaration of competing interest

The authors declare that they have no known competing financial interests or personal relationships that could have appeared to influence the work reported in this paper.

Data availability

Data will be made available on request.

Acknowledgements

Our study was supported in part by grants from the U.S. National Science Foundation (1911955, 2200310) and the Natural Science Foundation of China (42201341). We thank the editors and reviewers for their time and effort in reviewing our manuscript, and their comments and suggestions helped us to improve the manuscript.

Appendix A. Supplementary data

Supplementary data to this article can be found online at https://doi.org/10.1016/j.jenvman.2023.119618.

References

- Aiello-Lammens, M.E., Chu-Agor, M.L., Convertino, M., Fischer, R.A., Linkov, I., Resit Akçakaya, H., 2011. The impact of sea-level rise on S nowy P lovers in F lorida: integrating geomorphological, habitat, and metapopulation models. Global Change Biol. 17, 3644–3654.
- Amani, M., Mahdavi, S., Afshar, M., Brisco, B., Huang, W., Mohammad Javad Mirzadeh, S., White, L., Banks, S., Montgomery, J., Hopkinson, C., 2019. Canadian wetland inventory using Google Earth engine: the first map and preliminary results. Rem. Sens. 11, 842.
- Amani, M., Salehi, B., Mahdavi, S., Granger, J., Brisco, B., 2017. Wetland classification in Newfoundland and Labrador using multi-source SAR and optical data integration. GIScience Remote Sens. 54, 779–796.
- Beedy, E.C., 1981. Bird communities and forest structure in the Sierra Nevada of California. Condor 83, 97–105.
- Boto, K., Patrick Jr., W.H., 1979. Role of Wetlands in the Removal of Suspended Sediments. Wetland Functions and Values: the State of Our Understanding, pp. 479–489.
- Brix, H., Sorrell, B.K., Lorenzen, B., 2001. Are Phragmites-dominated wetlands a net source or net sink of greenhouse gases? Aquat. Bot. 69, 313–324.
- Chen, B., Xiao, X., Li, X., Pan, L., Doughty, R., Ma, J., Dong, J., Qin, Y., Zhao, B., Wu, Z., 2017. A mangrove forest map of China in 2015: analysis of time series Landsat 7/8 and Sentinel-1A imagery in Google Earth Engine cloud computing platform. ISPRS J. Photogrammetry Remote Sens. 131, 104–120.
- Chen, H., Zhang, W., Gao, H., Nie, N., 2018. Climate change and anthropogenic impacts on wetland and agriculture in the Songnen and Sanjiang Plain, Northeast China. Rem. Sens. 10, 356.
- Chu, Z., Guo, J., 2018. Effects of climatic change on maize varieties distribution in the future of Northeast China. J. Appl. Meteorol. Sci. 29, 165–176.
- Darrah, S.E., Shennan-Farpón, Y., Loh, J., Davidson, N.C., Finlayson, C.M., Gardner, R.C., Walpole, M.J., 2019. Improvements to the Wetland Extent Trends (WET) index as a tool for monitoring natural and human-made wetlands. Ecol. Indicat. 99, 294–298.
- Davidson, N.C., Finlayson, C.M., 2018. Extent, regional distribution and changes in area of different classes of wetland. Mar. Freshw. Res. 69, 1525–1533.
- Davranche, A., Lefebvre, G., Poulin, B., 2010. Wetland monitoring using classification trees and SPOT-5 seasonal time series. Rem. Sens. Environ. 114, 552–562.
- Dong, J., Xiao, X., Chen, B., Torbick, N., Jin, C., Zhang, G., Biradar, C., 2013. Mapping deciduous rubber plantations through integration of PALSAR and multi-temporal Landsat imagery. Rem. Sens. Environ. 134, 392–402.
- Dong, J., Xiao, X., Kou, W., Qin, Y., Zhang, G., Li, L., Jin, C., Zhou, Y., Wang, J., Biradar, C., 2015. Tracking the dynamics of paddy rice planting area in 1986–2010 through time series Landsat images and phenology-based algorithms. Rem. Sens. Environ. 160, 99–113.
- Dong, J., Xiao, X., Menarguez, M.A., Zhang, G., Qin, Y., Thau, D., Biradar, C., Moore III, B., 2016. Mapping paddy rice planting area in northeastern Asia with Landsat 8 images, phenology-based algorithm and Google Earth Engine. Rem. Sens. Environ. 185, 142–154.
- Farr, T.G., Rosen, P.A., Caro, E., Crippen, R., Duren, R., Hensley, S., Kobrick, M., Paller, M., Rodriguez, E., Roth, L., 2007. The shuttle radar topography mission. Rev. Geophys. 45.
- Geudtner, D., Torres, R., Snoeij, P., Davidson, M., Rommen, B., 2014. Sentinel-1 system capabilities and applications. In: 2014 IEEE Geoscience and Remote Sensing Symposium. IEEE, pp. 1457–1460.
- Ghosh, S., Mishra, D.R., Gitelson, A.A., 2016. Long-term monitoring of biophysical characteristics of tidal wetlands in the northern Gulf of Mexico—a methodological approach using MODIS. Rem. Sens. Environ. 173, 39–58.
- Gilbert, M., Golding, N., Zhou, H., Wint, G., Robinson, T.P., Tatem, A.J., Lai, S., Zhou, S., Jiang, H., Guo, D., 2014. Predicting the risk of avian influenza A H7N9 infection in live-poultry markets across Asia. Nat. Commun. 5, 1–7.
- Gilbert, M., Xiao, X., Pfeiffer, D.U., Epprecht, M., Boles, S., Czarnecki, C., Chaitaweesub, P., Kalpravidh, W., Minh, P.Q., Otte, M.J., 2008. Mapping H5N1 highly pathogenic avian influenza risk in Southeast Asia. Proc. Natl. Acad. Sci. USA 105, 4769–4774.

- Giri, C., Long, J., Abbas, S., Murali, R.M., Qamer, F.M., Pengra, B., Thau, D., 2015. Distribution and dynamics of mangrove forests of South Asia. J. Environ. Manag. 148, 101–111.
- Gong, P., Niu, Z., Cheng, X., Zhao, K., Zhou, D., Guo, J., Liang, L., Wang, X., Li, D., Huang, H., 2010. China's wetland change (1990–2000) determined by remote sensing. Sci. China Earth Sci. 53, 1036–1042.
- Gong, P., Wang, J., Yu, L., Zhao, Y., Zhao, Y., Liang, L., Niu, Z., Huang, X., Fu, H., Liu, S., 2013. Finer resolution observation and monitoring of global land cover: first mapping results with Landsat TM and ETM+ data. Int. J. Rem. Sens. 34, 2607–2654.
- Han, X., Pan, J., Devlin, A.T., 2018. Remote sensing study of wetlands in the Pearl River Delta during 1995–2015 with the support vector machine method. Front. Earth Sci. 12, 521–531
- Helman, D., Lensky, I.M., Tessler, N., Osem, Y., 2015. A phenology-based method for monitoring woody and herbaceous vegetation in Mediterranean forests from NDVI time series. Rem. Sens. 7, 12314–12335.
- Hemati, M., Hasanlou, M., Mahdianpari, M., Mohammadimanesh, F., 2023. Iranian wetland inventory map at a spatial resolution of 10 m using Sentinel-1 and Sentinel-2 data on the Google Earth Engine cloud computing platform. Environ. Monit. Assess. 195, 1–21.
- Hu, Y., Tian, B., Yuan, L., Li, X., Huang, Y., Shi, R., Jiang, X., Sun, C., 2021. Mapping coastal salt marshes in China using time series of Sentinel-1 SAR. ISPRS J. Photogrammetry Remote Sens. 173, 122–134.
- Huang, C., Zhang, C., 2022. Characterizing urban growth in Vientiane from 2000 to 2019 using time-series optical and SAR-based estimates of urban land. Int. J. Appl. Earth Obs. Geoinf. 109, 102798.
- Huang, C., Zhang, C., 2023. Time-series remote sensing of rice paddy expansion in the Yellow River Delta: Towards sustainable ecological conservation in the context of water scarcity. Rem. Sens. Ecol. Conserv. 9, 454–468.
- Huete, A., Didan, K., Miura, T., Rodriguez, E.P., Gao, X., Ferreira, L.G., 2002. Overview of the radiometric and biophysical performance of the MODIS vegetation indices. Rem. Sens. Environ. 83, 195–213.
- Huete, A., Liu, H., Batchily, K., Van Leeuwen, W., 1997. A comparison of vegetation indices over a global set of TM images for EOS-MODIS. Rem. Sens. Environ. 59, 440-451
- Jansen, A., Healey, M., 2003. Frog communities and wetland condition: relationships with grazing by domestic livestock along an Australian floodplain river. Biol. Conserv. 109, 207–219.
- Jourdain, E., Gauthier-Clerc, M., Bicout, D., Sabatier, P., 2007. Bird migration routes and risk for pathogen dispersion into western Mediterranean wetlands. Emerg. Infect. Dis. 13, 365.
- Karra, K., Kontgis, C., Statman-Weil, Z., Mazzariello, J.C., Mathis, M., Brumby, S.P., 2021. Global land use/land cover with Sentinel 2 and deep learning. In: 2021 IEEE International Geoscience and Remote Sensing Symposium IGARSS. IEEE, pp. 4704–4707.
- Krauss, W.K., Zhu, Z., Stagg, L.C., 2021. Managing wetlands to improve carbon sequestration. Eos 102. Published on. (Accessed 16 November 2021).
- Lan, X., Basu, S., Schwietzke, S., Bruhwiler, L.M., Dlugokencky, E.J., Michel, S.E., Sherwood, O.A., Tans, P.P., Thoning, K., Etiope, G., 2021. Improved constraints on global methane emissions and sinks using 813C-CH4. Global Biogeochem. Cycles 35, e2021GB007000.
- Li, H., Fu, D., Huang, C., Su, F., Liu, Q., Liu, G., Wu, S., 2020. An approach to highresolution rice paddy mapping using time-series Sentinel-1 SAR data in the Mun River Basin, Thailand. Rem. Sens. 12, 3959.
- Linderholm, H.W., Walther, A., Chen, D., 2008. Twentieth-century trends in the thermal growing season in the Greater Baltic Area. Climatic Change 87, 405–419.
- Liu, M., Li, H., Li, L., Man, W., Jia, M., Wang, Z., Lu, C., 2017. Monitoring the invasion of Spartina alterniflora using multi-source high-resolution imagery in the Zhangjiang Estuary, China. Rem. Sens. 9, 539.
- Loveland, T.R., Reed, B.C., Brown, J.F., Ohlen, D.O., Zhu, Z., Yang, L., Merchant, J.W., 2000. Development of a global land cover characteristics database and IGBP DISCover from 1 km AVHRR data. Int. J. Rem. Sens. 21, 1303–1330.
- Mahdianpari, M., Salehi, B., Mohammadimanesh, F., Brisco, B., Homayouni, S., Gill, E., DeLancey, E.R., Bourgeau-Chavez, L., 2020. Big data for a big country: the first generation of Canadian wetland inventory map at a spatial resolution of 10-m using Sentinel-1 and Sentinel-2 data on the Google Earth Engine cloud computing platform. Can. J. Rem. Sens. 46, 15–33.
- Mao, D., Wang, Z., Du, B., Li, L., Tian, Y., Jia, M., Zeng, Y., Song, K., Jiang, M., Wang, Y., 2020. National wetland mapping in China: a new product resulting from objectbased and hierarchical classification of Landsat 8 OLI images. ISPRS J. Photogrammetry Remote Sens. 164, 11–25.
- Martinis, S., Rieke, C., 2015. Backscatter analysis using multi-temporal and multi-frequency SAR data in the context of flood mapping at River Saale, Germany. Rem. Sens. 7, 7732–7752.
- Massey, R., Sankey, T.T., Congalton, R.G., Yadav, K., Thenkabail, P.S., Ozdogan, M., Meador, A.J.S., 2017. MODIS phenology-derived, multi-year distribution of conterminous US crop types. Rem. Sens. Environ. 198, 490–503.
- Mehner, T., 2009. Encyclopedia of Inland Waters. Academic Press.
- Murray, N.J., Phinn, S.R., DeWitt, M., Ferrari, R., Johnston, R., Lyons, M.B., Clinton, N., Thau, D., Fuller, R.A., 2019. The global distribution and trajectory of tidal flats. Nature 565, 222–225.
- Niculescu, S., Boissonnat, J.-B., Lardeux, C., Roberts, D., Hanganu, J., Billey, A., Constantinescu, A., Doroftei, M., 2020. Synergy of high-resolution radar and optical images satellite for identification and mapping of wetland macrophytes on the Danube Delta. Rem. Sens. 12, 2188.

- Niu, Z., Gong, P., Cheng, X., Guo, J., Wang, L., Huang, H., Shen, S., Wu, Y., Wang, X., Wang, X., 2009. Geographical characteristics of China's wetlands derived from remotely sensed data. Sci. China Earth Sci. 52, 723–738.
- Onojeghuo, A.O., Onojeghuo, A.R., Cotton, M., Potter, J., Jones, B., 2021. Wetland mapping with multi-temporal sentinel-1 &-2 imagery (2017–2020) and LiDAR data in the grassland natural region of alberta. GIScience Remote Sens. 58, 999–1021.
- Pahlevan, N., Chittimalli, S.K., Balasubramanian, S.V., Vellucci, V., 2019. Sentinel-2/ Landsat-8 product consistency and implications for monitoring aquatic systems. Rem. Sens. Environ. 220, 19–29.
- Panda, B.P., Das, A.K., Jena, S.K., Mahapatra, B., Dash, A.K., Pradhan, A., Parida, S.P., 2021. Habitat heterogeneity and seasonal variations influencing avian community structure in wetlands. J. Asia Pac. Bus. 14, 23–32.
- Parmuchi, M.G., Karszenbaum, H., Kandus, P., 2002. Mapping wetlands using multitemporal RADARSAT-1 data and a decision-based classifier. Can. J. Rem. Sens. 28, 175–186
- Picek, T., Čížková, H., Dušek, J., 2007. Greenhouse gas emissions from a constructed wetland—plants as important sources of carbon. Ecol. Eng. 31, 98–106.
- Pickens, A.H., Hansen, M.C., Hancher, M., Stehman, S.V., Tyukavina, A., Potapov, P., Marroquin, B., Sherani, Z., 2020. Mapping and sampling to characterize global inland water dynamics from 1999 to 2018 with full Landsat time-series. Rem. Sens. Environ. 243, 111792.
- Qin, Y., Xiao, X., Dong, J., Chen, B., Liu, F., Zhang, G., Zhang, Y., Wang, J., Wu, X., 2017. Quantifying annual changes in built-up area in complex urban-rural landscapes from analyses of PALSAR and Landsat images. ISPRS J. Photogrammetry Remote Sens. 124, 89–105.
- Qin, Y., Xiao, X., Dong, J., Zhang, G., Shimada, M., Liu, J., Li, C., Kou, W., Moore III, B., 2015. Forest cover maps of China in 2010 from multiple approaches and data sources: PALSAR, Landsat, MODIS, FRA, and NFI. ISPRS J. Photogrammetry Remote Sens. 109, 1–16.
- Richards, D.R., Friess, D.A., 2016. Rates and drivers of mangrove deforestation in Southeast Asia, 2000–2012. Proc. Natl. Acad. Sci. USA 113, 344–349.
- Sandoval, L., Zamora-Castro, S.A., Vidal-Álvarez, M., Marín-Muñiz, J.L., 2019. Role of wetland plants and use of ornamental flowering plants in constructed wetlands for wastewater treatment: a review. Appl. Sci. 9, 685.
- Shimada, M., Itoh, T., Motooka, T., Watanabe, M., Shiraishi, T., Thapa, R., Lucas, R., 2014. New global forest/non-forest maps from ALOS PALSAR data (2007–2010). Rem. Sens. Environ. 155, 13–31.
- Simard, M., Grandi, G.D., Saatchi, S., Mayaux, P., 2002. Mapping tropical coastal vegetation using JERS-1 and ERS-1 radar data with a decision tree classifier. Int. J. Rem. Sens. 23. 1461–1474.
- Simard, M., Rivera-Monroy, V.H., Mancera-Pineda, J.E., Castañeda-Moya, E., Twilley, R. R., 2008. A systematic method for 3D mapping of mangrove forests based on Shuttle Radar Topography Mission elevation data, ICEsat/GLAS waveforms and field data: application to Ciénaga Grande de Santa Marta, Colombia. Rem. Sens. Environ. 112, 2131–2144.
- Slagter, B., Tsendbazar, N.-E., Vollrath, A., Reiche, J., 2020. Mapping wetland characteristics using temporally dense Sentinel-1 and Sentinel-2 data: a case study in the St. Lucia wetlands, South Africa. Int. J. Appl. Earth Obs. Geoinf. 86, 102009.
- Son, N.-T., Chen, C.-F., Chen, C.-R., Duc, H.-N., Chang, L.-Y., 2014. A phenology-based classification of time-series MODIS data for rice crop monitoring in Mekong Delta, Vietnam. Rem. Sens. 6, 135–156.
- Song, M., Civco, D., Hurd, J., 2005. A competitive pixel-object approach for land cover classification. Int. J. Rem. Sens. 26, 4981–4997.
- Tanalgo, K.C., Pineda, J.A.F., Agravante, M.E., Amerol, Z.M., 2015. Bird diversity and structure in different land-use types in lowland south-central Mindanao, Philippines. Trop. Life Sci. Res. 26, 85.
- $\label{total condition} Tollefson, J., 2022. Scientists raise alarm over dangerously fast growth in atmospheric methane. Nature.$ <math display="block"> https://doi.org/10.1038/d41586-022-00312-2.
- Torres, R., Snoeij, P., Geudtner, D., Bibby, D., Davidson, M., Attema, E., Potin, P., Rommen, B., Floury, N., Brown, M., 2012. GMES Sentinel-1 mission. Rem. Sens. Environ. 120, 9–24.
- Townsend, P., 2002. Relationships between forest structure and the detection of flood inundation in forested wetlands using C-band SAR. Int. J. Rem. Sens. 23, 443–460.
- Tucker, C.J., 1979. Red and photographic infrared linear combinations for monitoring vegetation. Rem. Sens. Environ. 8, 127–150.
- Vo, Q.T., Oppelt, N., Leinenkugel, P., Kuenzer, C., 2013. Remote sensing in mapping mangrove ecosystems—an object-based approach. Rem. Sens. 5, 183–201.
- Wan, Z., 2008. New refinements and validation of the MODIS land-surface temperature/ emissivity products. Rem. Sens. Environ. 112, 59–74.
- Wang, J., Xiao, X., Liu, L., Wu, X., Qin, Y., Steiner, J.L., Dong, J., 2020a. Mapping sugarcane plantation dynamics in Guangxi, China, by time series Sentinel-1, Sentinel-2 and Landsat images. Rem. Sens. Environ. 247, 111951.

- Wang, L., Sousa, W.P., Gong, P., Biging, G.S., 2004. Comparison of IKONOS and QuickBird images for mapping mangrove species on the Caribbean coast of Panama. Rem. Sens. Environ. 91, 432–440.
- Wang, T., Zhang, H., Lin, H., Fang, C., 2015. Textural–spectral feature-based species classification of mangroves in Mai Po Nature Reserve from Worldview-3 imagery. Rem. Sens. 8, 24.
- Wang, X., Xiao, X., Xu, X., Zou, Z., Chen, B., Qin, Y., Zhang, X., Dong, J., Liu, D., Pan, L., 2021. Rebound in China's coastal wetlands following conservation and restoration. Nat. Sustain. 4, 1076–1083.
- Wang, X., Xiao, X., Zou, Z., Chen, B., Ma, J., Dong, J., Doughty, R.B., Zhong, Q., Qin, Y., Dai, S., 2020b. Tracking annual changes of coastal tidal flats in China during 1986–2016 through analyses of Landsat images with Google Earth Engine. Rem. Sens. Environ. 238, 110987.
- Wang, X., Xiao, X., Zou, Z., Dong, J., Qin, Y., Doughty, R.B., Menarguez, M.A., Chen, B., Wang, J., Ye, H., 2020c. Gainers and losers of surface and terrestrial water resources in China during 1989–2016. Nat. Commun. 11, 1–12.
- Wang, X., Xiao, X., Zou, Z., Hou, L., Qin, Y., Dong, J., Doughty, R.B., Chen, B., Zhang, X., Chen, Y., 2020d. Mapping coastal wetlands of China using time series Landsat images in 2018 and Google Earth Engine. ISPRS J. Photogrammetry Remote Sens. 163, 312–326.
- Xiao, X., Boles, S., Frolking, S., Li, C., Babu, J.Y., Salas, W., Moore III, B., 2006. Mapping paddy rice agriculture in South and Southeast Asia using multi-temporal MODIS images. Rem. Sens. Environ. 100, 95–113.
- Xiao, X., Boles, S., Liu, J., Zhuang, D., Frolking, S., Li, C., Salas, W., Moore III, B., 2005a. Mapping paddy rice agriculture in southern China using multi-temporal MODIS images. Rem. Sens. Environ. 95, 480–492.
- Xiao, X., He, L., Salas, W., Li, C., Moore Iii, B., Zhao, R., Frolking, S., Boles, S., 2002. Quantitative relationships between field-measured leaf area index and vegetation index derived from VEGETATION images for paddy rice fields. Int. J. Rem. Sens. 23, 3595–3604.
- Xiao, X., Hollinger, D., Aber, J., Goltz, M., Davidson, E.A., Zhang, Q., Moore III, B., 2004. Satellite-based modeling of gross primary production in an evergreen needleleaf forest. Rem. Sens. Environ. 89, 519–534.
- Xiao, X., Zhang, Q., Hollinger, D., Aber, J., Moore III, B., 2005b. Modeling gross primary production of an evergreen needleleaf forest using MODIS and climate data. Ecol. Appl. 15, 954–969.
- Xing, L., Niu, Z., 2019. Mapping and analyzing China's wetlands using MODIS time series data. Wetl. Ecol. Manag. 27, 693–710.
- Xu, H., 2006. Modification of normalised difference water index (NDWI) to enhance open water features in remotely sensed imagery. Int. J. Rem. Sens. 27, 3025–3033.
- Zhang, C., Xiao, X., Zhao, L., Qin, Y., Doughty, R., Wang, X., Dong, J., Yang, X., 2023a. Mapping Eucalyptus plantation in Guangxi, China by using knowledge-based algorithms and PALSAR-2, Sentinel-2, and Landsat images in 2020. Int. J. Appl. Earth Obs. Geoinf. 120. 103348.
- Zhang, G., Xiao, X., Dong, J., Kou, W., Jin, C., Qin, Y., Zhou, Y., Wang, J., Menarguez, M. A., Biradar, C., 2015. Mapping paddy rice planting areas through time series analysis of MODIS land surface temperature and vegetation index data. ISPRS J. Photogrammetry Remote Sens. 106, 157–171.
- Zhang, M., Lin, H., 2022. Wetland classification using parcel-level ensemble algorithm based on Gaofen-6 multispectral imagery and Sentinel-1 dataset. J. Hydrol. 606, 127462
- Zhang, X., Liu, L., Chen, X., Gao, Y., Xie, S., Mi, J., 2021. GLC FCS30: global land-cover product with fine classification system at 30 m using time-series Landsat imagery. Earth Syst. Sci. Data 13, 2753–2776.
- Zhang, X., Liu, L., Zhao, T., Chen, X., Lin, S., Wang, J., Mi, J., Liu, W., 2023b. GWL_FCS30: a global 30 m wetland map with a fine classification system using multisourced and time-series remote sensing imagery in 2020. Earth Syst. Sci. Data 15, 265–293.
- Zhang, X., Xiao, X., Qiu, S., Xu, X., Wang, X., Chang, Q., Wu, J., Li, B., 2022. Quantifying latitudinal variation in land surface phenology of Spartina alterniflora saltmarshes across coastal wetlands in China by Landsat 7/8 and Sentinel-2 images. Rem. Sens. Environ. 269, 112810.
- Zhang, X., Xiao, X., Wang, X., Xu, X., Chen, B., Wang, J., Ma, J., Zhao, B., Li, B., 2020. Quantifying expansion and removal of Spartina alterniflora on Chongming island, China, using time series Landsat images during 1995–2018. Rem. Sens. Environ. 247, 111916.
- Zhou, Y., Xiao, X., Qin, Y., Dong, J., Zhang, G., Kou, W., Jin, C., Wang, J., Li, X., 2016.
 Mapping paddy rice planting area in rice-wetland coexistent areas through analysis of Landsat 8 OLI and MODIS images. Int. J. Appl. Earth Obs. Geoinf. 46, 1–12.
- Zhu, Z., Woodcock, C.E., 2012. Object-based cloud and cloud shadow detection in Landsat imagery. Rem. Sens. Environ. 118, 83–94.
- Zou, Z., Xiao, X., Dong, J., Qin, Y., Doughty, R.B., Menarguez, M.A., Zhang, G., Wang, J., 2018. Divergent trends of open-surface water body area in the contiguous United States from 1984 to 2016. Proc. Natl. Acad. Sci. USA 115, 3810–3815.